

Article

# Investigation of the Dynamic Recovery and Recrystallization of Near- $\beta$ Titanium Alloy Ti-55511 during Two-Pass Hot Compression

Hande Wang, Jinyang Ge, Xiaoyong Zhang \*, Chao Chen \*  and Kechao Zhou

State Key Laboratory of Powder Metallurgy, Central South University, Lu Mountain South Road, Changsha 410083, China; 183312092@csu.edu.cn (H.W.); gjy416065@126.com (J.G.); zhoukechao@csu.edu.cn (K.Z.)

\* Correspondence: zhangxiaoyong@csu.edu.cn (X.Z.); pkhqchenchao@126.com (C.C.)

**Abstract:** The two-pass thermal compression behavior of near- $\beta$  Ti-55511 alloy was investigated. The first-pass restoration mechanisms changed from dynamic recrystallization (DRX) to dynamic recovery (DRV) as the first-pass deformation temperature increased from 700 °C to 850 °C. The occurrence of recrystallization reduced the dislocation density, resulting in a slower grain growth rate in the subsequent process. Because of the static recrystallization (SRX) and  $\beta$  grain growth, the  $\beta$  grain size increased and the morphology became less uniform during the subsequent  $\beta$  holding process, which also changed the restoration mechanism during second-pass compression. The level of continuous dynamic recrystallization (CDRX) and discontinuous dynamic recrystallization (DDRX) become weaker during second-pass deformation. The changes in the restoration mechanism and the microstructures slightly increased the peak stress during the second-pass deformation.

**Keywords:** near- $\beta$  titanium alloy; two-pass hot compression; dynamic recovery (DRV); continuous dynamic recrystallization (CDRX); discontinuous dynamic recrystallization (DDRX)



**Citation:** Wang, H.; Ge, J.; Zhang, X.; Chen, C.; Zhou, K. Investigation of the Dynamic Recovery and Recrystallization of Near- $\beta$  Titanium Alloy Ti-55511 during Two-Pass Hot Compression. *Metals* **2021**, *11*, 359. <https://doi.org/10.3390/met11020359>

Academic Editor: Artur Shugurov

Received: 1 February 2021  
Accepted: 17 February 2021  
Published: 20 February 2021

**Publisher's Note:** MDPI stays neutral with regard to jurisdictional claims in published maps and institutional affiliations.



**Copyright:** © 2021 by the authors. Licensee MDPI, Basel, Switzerland. This article is an open access article distributed under the terms and conditions of the Creative Commons Attribution (CC BY) license (<https://creativecommons.org/licenses/by/4.0/>).

## 1. Introduction

Near- $\beta$  titanium Ti-55511 is a high-strength lightweight alloy with good fatigue performance that is widely used in the aerospace field [1–3]. The mechanical properties of the Ti-55511 alloy are closely related to its microstructure [4,5]. In general, titanium alloys with a fine microstructure have better mechanical properties than those with coarse microstructures [6]. Forging is a widely used industrial grain refinement method [7]. Deformation parameters, such as temperature, strain rate, and strain, play important roles during thermal forging [8–11]. For example, reducing the deformation temperature in the  $\alpha + \beta$  region can effectively reduce the  $\beta$  grain size [10], but this is not conducive to grain refinement in the  $\beta$  region [12]. A relatively low strain rate and large strain are favorable for the recrystallization of  $\beta$  grains, which promotes  $\beta$  grain refinement [13]; however, it is very difficult to process titanium alloys by single-pass large plastic deformation due to the large deformation resistance [8]. Multi-pass deformation was developed to efficiently process titanium alloys. Zhan et al. [14] found that grain refinement occurred by multi-pass deformation, and the contents of  $<5 \mu\text{m}$   $\beta$  grains increased significantly upon increasing the number of compression passes from 1 to 5 at 800 °C. Zherebtsov et al. [10] found that the deformation temperature during subsequent passes could be reduced appropriately because the workability was improved after the previous pass deformation. The grain size was reduced by decreasing the deformation temperature, and ultrafine grains with an average size of 150 nm were obtained at a deformation temperature of 475 °C. To obtain fine and homogeneous  $\beta$  grains, a “high-low-high” process was proposed which involved primary working in the  $\beta$  region, followed by working in the  $\alpha + \beta$  region, and finally  $\beta$  working again [15].

Dynamic recovery (DRV) and dynamic recrystallization (DRX) are the main mechanisms that influence the grain refinement during multi-pass deformation, and they are very sensitive to the deformation temperature [13,16]. Warchomicka et al. [13] found that DRV is the dominant restoration mechanism at the beginning of deformation. Subsequently, geometric dynamic recrystallization (GDRX) occurs below the  $\beta$  transition temperature, while continuous dynamic recrystallization (CDRX) occurs above the  $\beta$  transition temperature. The emergence of DRV and DRX influences the microstructure deformation. Ning et al. [17] found that the periodic competition between DRX and DRV resulted in the incomplete growth of recrystallized grains. Different initial microstructures also produce differences in the restoration behavior. For example, Wu et al. [18] found that, since the recrystallization rate of the deformed microstructure is significantly higher than that of the undeformed microstructure,  $\beta$  grains were refined during subsequent deformation. Dehghan-Manshadi et al. [19] found that the recrystallization mechanism changed from DDRX to CDRX upon decreasing the initial grain size.

The fundamental factors affecting recrystallization are nucleation and growth rate, which are related to the dislocation density [20]. The  $\alpha$  phase plays an important role in the movement and entanglement of dislocations because it has limited slip systems during deformation [21]. As a result, dislocations are more likely to accumulate around  $\alpha$  precipitates, which then promote  $\beta$  grain nucleation and inhibit  $\beta$  grain growth [22,23]. Moreover, recrystallization can be improved by changing the  $\alpha$  morphology before deformation [11,21]. The typical initial microstructures, lamellar and equiaxed, have different effects on the dislocation motion. Wei et al. [24] found that dislocations more easily accumulated around equiaxed  $\alpha$  grains and then formed high-angle grain boundaries after hot-rolling with a strain of 80% at 750 °C. As a result, the size of the  $\beta$  grain with an initial equiaxed  $\alpha$  microstructure was finer than that with an initial lamellar  $\alpha$  microstructure. On the other hand, more slip systems were activated by increasing the number of deformation passes in which the slip mode changed from base slip to pyramid slip [25]. Multi-pass deformation leads to a higher dislocation density and makes it easier to form finer grains in the  $\beta$  matrix [26].

Previous research on the recrystallization mechanism has mainly focused on single-pass deformation. Multi-pass forging is the main processing method of Ti-55511 ingots, and there is limited research on the interactions between deformation mechanisms during multi-pass deformation. In this study, four types of two-pass hot compression methods were designed to investigate the influence of the first-pass deformation restoration behavior on subsequent deformation. This work for Ti-55511 provides essential references for process parameter optimizing and microstructure controlling under multi-pass forging conditions.

## 2. Materials and Methods

Ti-55511 ingot with the composition (wt%) of 5.16 Al, 4.92 Mo, 4.96 V, 1.10 Cr, 0.98 Fe, and Ti (balance) was provided by Xiangtou Goldsky Titanium Industry (Changde, Hunan, China). The  $\beta$ -transition temperature was found to be approximately 875 °C using the metallographic method. Figure 1 shows the original microstructure composed of large  $\beta$  grains with an average size of 300  $\mu\text{m}$ . Inside  $\beta$  grains, there are  $\alpha$  duplex microstructures including (1) an equiaxed  $\alpha$  grain with a diameter of 5–8  $\mu\text{m}$  and (2) a lamellar  $\alpha$  grain with a length of 3–5  $\mu\text{m}$ .

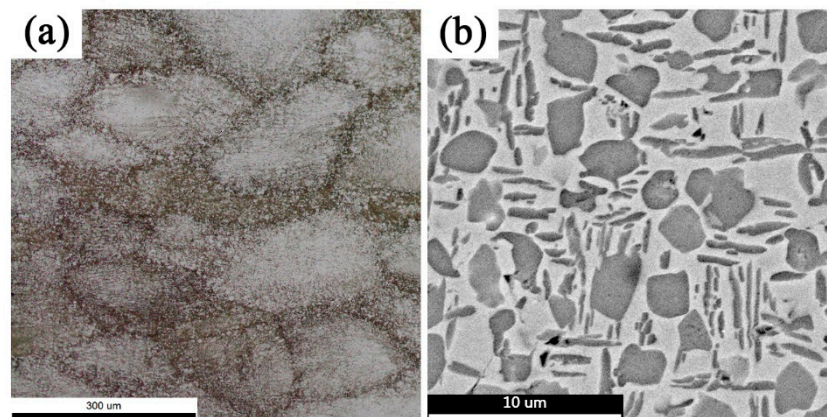


**Figure 1.** (a) Metallographic image and (b) SEM image of the original microstructure of Ti-55511.

Samples of  $\Phi 10 \times 15$  mm sizes were line-cut from an ingot and then mechanically polished. Thermal compression was conducted on a Gleeble 3800 thermo-mechanical simulator (Data sciences international, INC, New Brighton, MN, USA) at a strain rate of  $0.1 \text{ s}^{-1}$ , including three stages as shown in Figure 2: (1) compression to a true strain of 0.36 at 700–850 °C, followed by water quenching (Stage-D1); (2) heating to 950 °C and holding for 3 min (Stage-H); (3) continuing to compress at a true strain of 0.56 and then water quenching (Stage-D2). During compression, tantalum wafers, which play the role of a lubricant, were placed between the samples and die to maintain uniform deformation. Thermocouples were welded to samples to measure the processing temperatures.

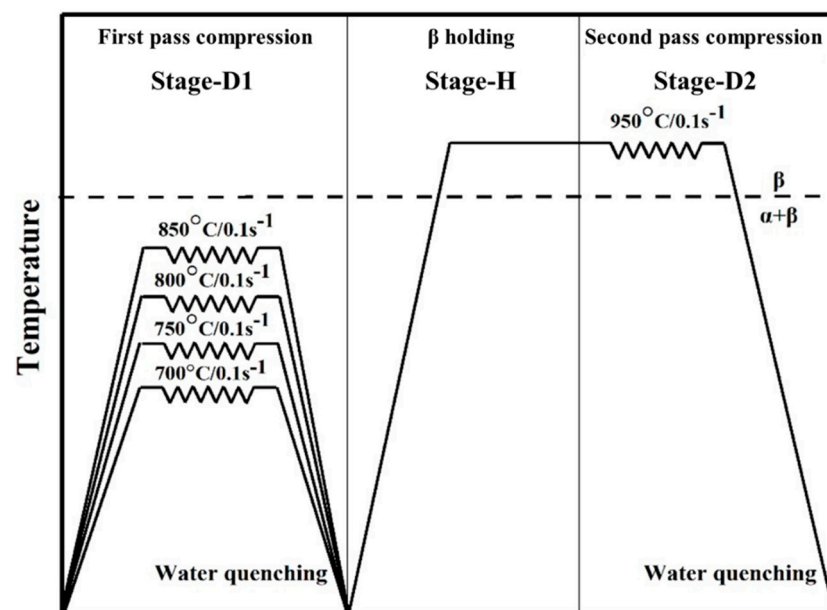


**Figure 2.** Schematic diagram of the thermal compression process.

The hot-compressed samples were cut along the compression direction using electro-discharge machining. Then, they were mechanically ground by SiC paper and finally polished by a twin-jet electropolisher at a  $-30$  °C surrounding temperature and 30 V operating voltage. Specimens were jet-thinned by Kroll's reagent, which was composed of 300 mL methanol, 175 mL N-butyl alcohol, and 25 mL perchlorate acid.

The microstructure of the compressed samples was characterized by scanning electron microscope (SEM) (FEI Czech Republic s.r.o., Brno, Czech Republic) and electron backscattered diffraction (EBSD) (FEI Czech Republic s.r.o., Brno, Czech Republic) using  $0.2 \mu\text{m}$  and  $0.6 \mu\text{m}$  step sizes and a 20 kV operating voltage. Information about the misorientation

and dislocation density was obtained by data analysis using the OIM software (EDAX). All the samples were obtained from the center of each compression sample.

### 3. Results and Discussion

#### 3.1. Flow Behavior

Figure 3a depicts the stress–strain curves of the first-pass deformation at a strain rate of  $0.1 \text{ s}^{-1}$ . The stress quickly reaches the peak in the early stage of the first-pass deformation. The deformation temperature has a great influence on the flow behavior, and the peak stress decreases upon increasing the deformation temperature. A higher deformation temperature leads to a lower  $\alpha$ -phase content and more operative slip systems [27,28]. After the peak stress, the curve decreases significantly at a strain of 0.12 in the 700 °C first compression sample; however, the curves at other deformation temperatures quickly reach a steady state after passing the peak stress.

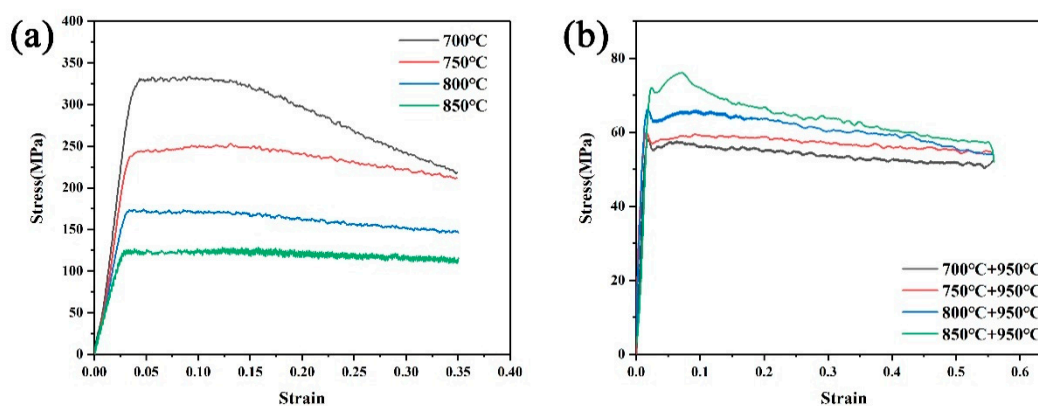


Figure 3. Stress-strain curves of duplex Ti-55511 during (a) first-pass and (b) second-pass thermal compression.

Figure 3b shows the stress–strain curves of the second-pass compression. The peak stress of the second-pass deformation increases upon increasing the deformation temperature during first-pass deformation. Obvious discontinuous yielding also appears due to recrystallization, which is closely related to the generation of movable dislocations [19,29]. After the discontinuous yield phenomenon, limited work-hardening is observed, and then flow stress enters the steady stage. The flow oscillation phenomenon is still obvious in this stage, which indicates the promoting of DRX after the first-pass compression [16].

#### 3.2. Microstructure Characteristics after First-Pass Compression (Stage-D1)

Figure 4a–d show the microstructure characteristics after first-pass compression. In Figure 4a, the fine lamellar  $\alpha$  phase is uniformly distributed among the equiaxed  $\alpha$  phase. The average lamellar  $\alpha$  phase is 3–5  $\mu\text{m}$  long, and the average equiaxed  $\alpha$  phase radius is about 5  $\mu\text{m}$ . When the deformation temperature reaches 750 °C, the lamellar  $\alpha$  phase disappears and only the equiaxed  $\alpha$  phase exists in the matrix. The sample deformed at 750 °C contains less  $\alpha$  phase. Upon further increasing the deformation temperature, the content of  $\alpha$  phase continues to decrease, and the equiaxed  $\alpha$  phase becomes smaller.

To reveal the change in the  $\beta$  matrix, Figure 5 shows the inverse pole figures (IPF) at different deformation temperatures. High-angle grain boundaries (HAGBs; misorientation angle  $>15^\circ$ ) and low-angle grain boundaries (LAGBs;  $2^\circ < \text{misorientation angle} < 15^\circ$ ) are represented by black and white lines, respectively. Figure 5a shows that a large number of HAGBs appear at the  $\alpha/\beta$  interface due to the occurrence of DRX, which explains the sudden drop of stress in the strain–stress curve mentioned earlier (Figure 4a); however, the recrystallization is still in the early stage, and the recrystallized grain is only a few microns in size. Figure 5b shows that at 750 °C, the LAGBs are uniformly distributed in the matrix and the LAGB fraction reaches 0.99, which means that the dominant restoration mechanism changes to DRV at 750 °C. However, in some regions (circled areas in Figure 5b)

a small number of recrystallized grains form in the  $\alpha$  grooves. Upon increasing the deformation temperature, the content of LAGBs in the  $\beta$  matrix continuously decreases, and no recrystallized grains are observed in the  $\beta$  matrix. The deformation process is mainly controlled by the DRV mechanism, and the level of DRV gradually decreases.

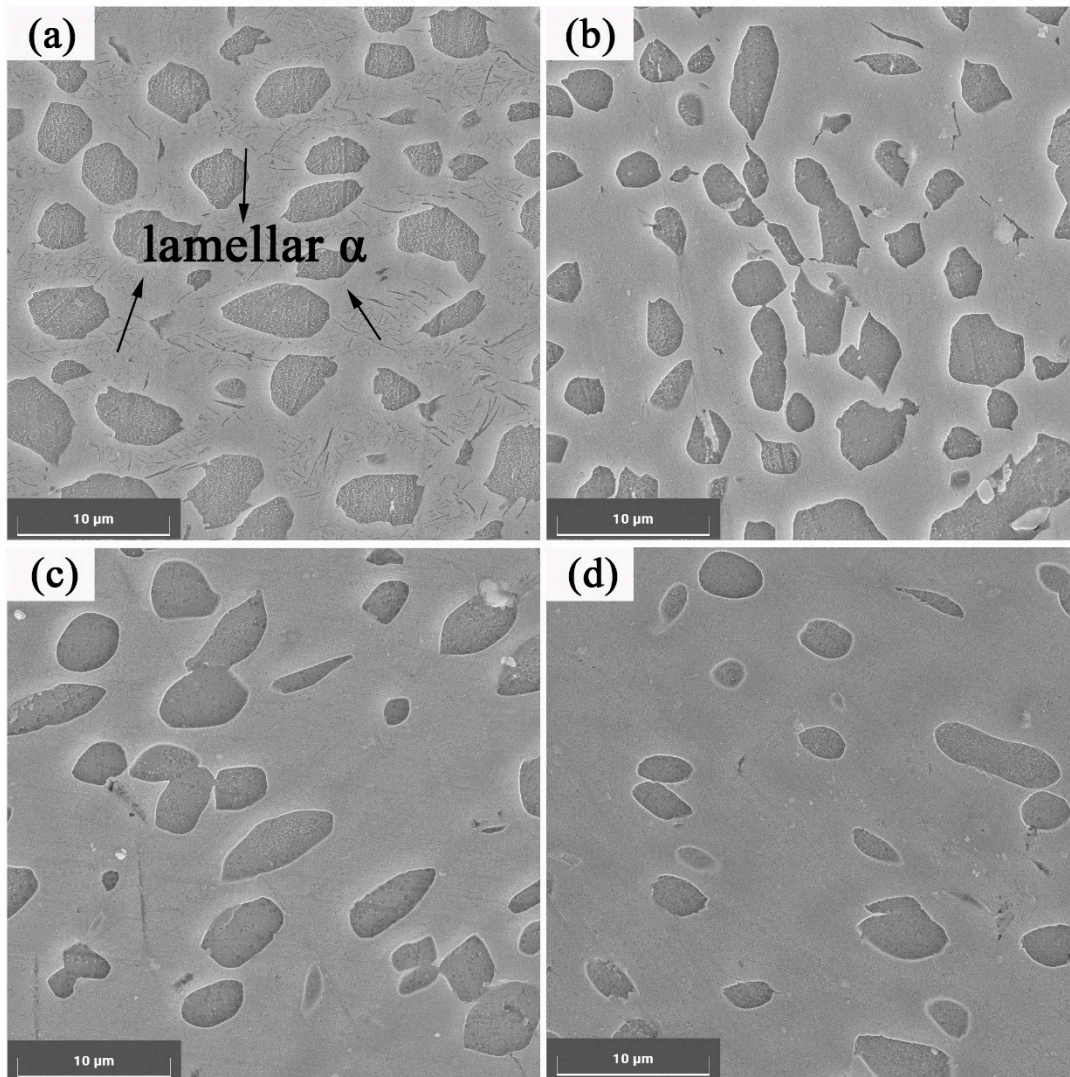


**Figure 4.** SEM figures after first-pass compression at (a) 700 °C, (b) 750 °C, (c) 800 °C, (d) 850 °C.

DRX and DRV are related to the dislocation density. To reveal the dislocation distribution, kernel average misorientation (KAM) maps were obtained, as shown in Figure 6. A higher KAM value indicates a higher dislocation content and more severe deformation. In Figure 6a, the KAM value at 700 °C is lower than at other temperatures because the recrystallization effectively eliminates the residual dislocations in deformed grains [30,31]. The different dislocation densities affect the growth rate of recrystallized grains during subsequent holding.

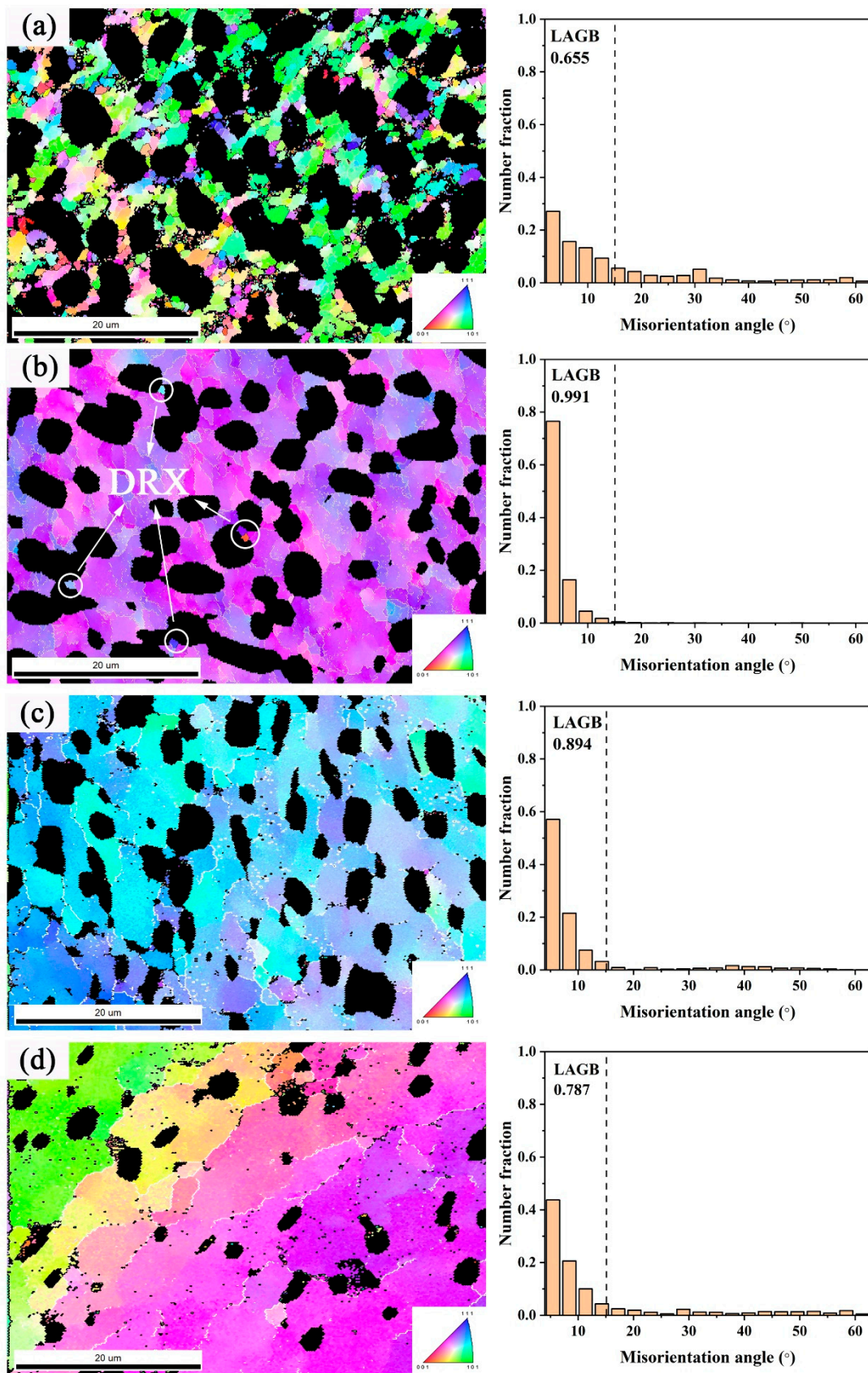
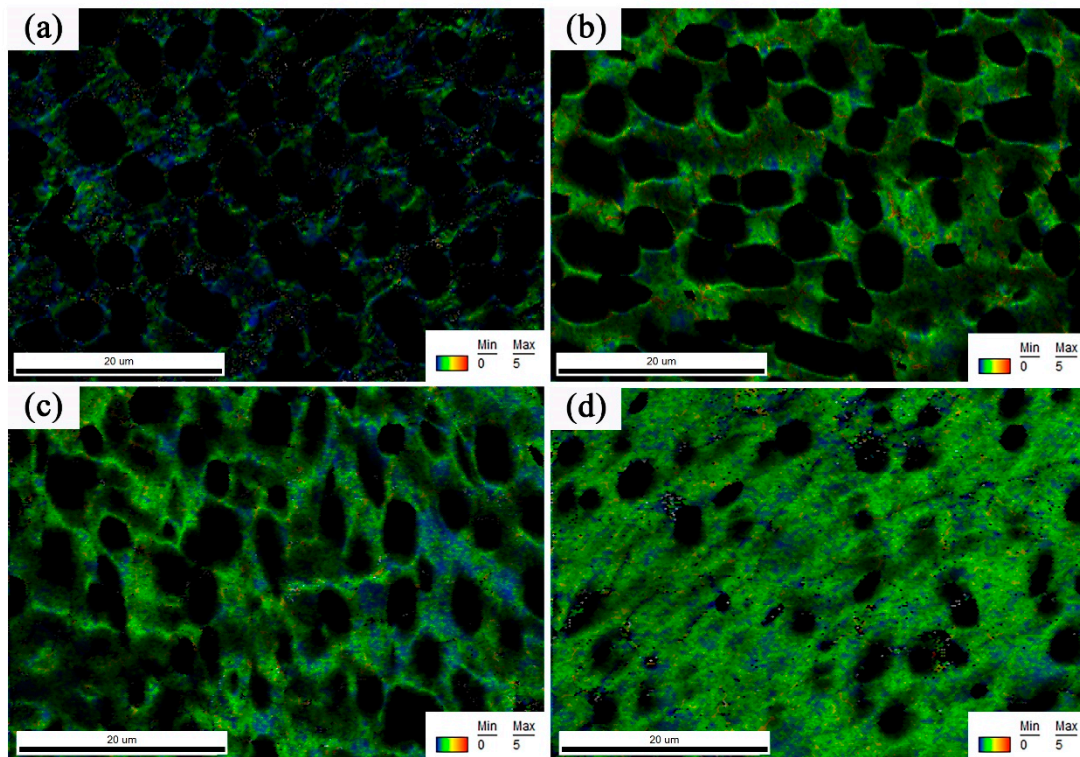


Figure 5. Inverse pole figures (IPF) figures after first-pass compression at (a) 700 °C, (b) 750 °C, (c) 800 °C, (d) 850 °C.



**Figure 6.** Kernel average misorientation (KAM) figures of samples after first-pass compression at (a) 700 °C, (b) 750 °C, (c) 800 °C, (d) 850 °C.

### 3.3. Microstructure Characteristics after Holding at 950 °C (Stage-H)

Figure 7a shows the sample microstructure after being deformed at 700 °C and then holding at 950 °C for 3 min. The  $\beta$  grain boundaries show zigzag lines, and the  $\beta$  grain size is significantly finer than that of other samples. This is because the  $\beta$  grain size is related to the recrystallization nucleation rate and the grain boundary migration rate [32]. A high nucleation rate and a small grain boundary migration rate are conducive to grain refinement. Meanwhile, the rate of grain boundary migration ( $v$ ) and the effective pressure ( $P_{Eff}$ ) on the grain boundary satisfy equation:

$$v = mP_{Eff}, \quad (1)$$

where effective pressure ( $P_{Eff}$ ) is the sum of driving pressure ( $P_D$ ) and retarding pressure ( $P_R$ ). Driving pressure ( $P_D$ ) is related to dislocation density:

$$P_D = (\rho_2 - \rho_1)\tau, \quad (2)$$

where  $\tau$  is the energy of per unit length dislocation and  $\rho$  is the dislocation density. A large amount of recrystallized nucleation has been observed in the sample deformed at 700 °C, and the generation of  $\beta$  recrystallized grains reduces the dislocation density in the  $\beta$  matrix. This results in the  $\beta$  grain size in Figure 7a being much smaller than that of other samples. The microstructure of the sample after deforming at 750 °C and holding at 950 °C for 3 min is shown in Figure 7b. The average crystal grain size greatly increases to 128  $\mu\text{m}$  and the grain boundaries become straight. Compared with the sample deformed at 700 °C, the average dislocation density is higher, which leads to the rapid growth of the recrystallized grains. The circled small grains are observed at the junction of boundaries where dislocation plugging drives the generation of SRX. In addition, some sub-crystals still exist in the matrix (arrows in Figure 7) because the strain of the first-pass deformation

is only 0.36, which provides insufficient deformation storage energy to convert all LAGBs to HAGBs.

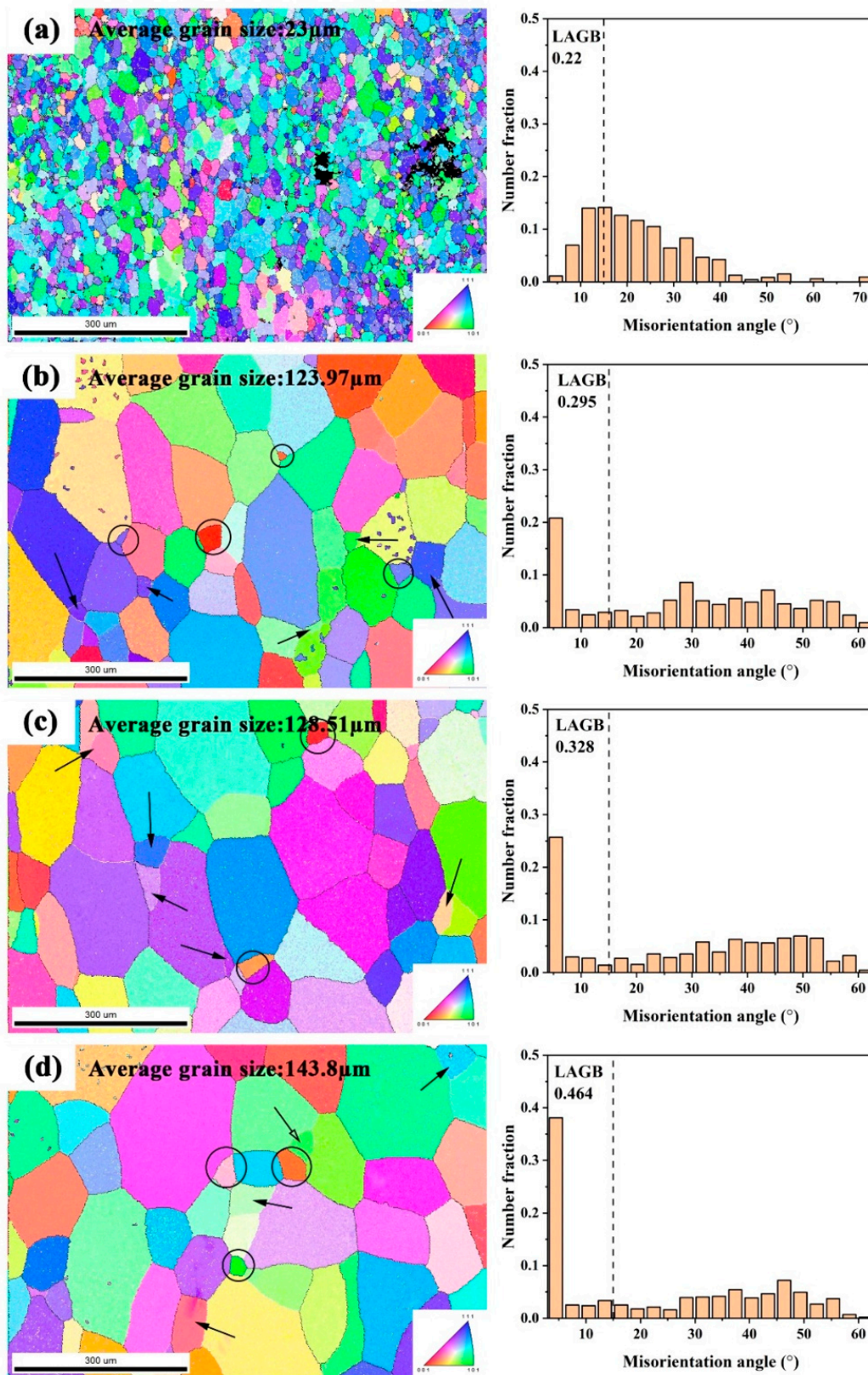


**Figure 7.** Electron backscattered diffraction (EBSD) figures after (a) 700 °C, (b) 750 °C, (c) 800 °C, (d) 850 °C first-pass compressing and then holding at 950 °C for 3 min.

As the first-pass deformation temperature constantly increases, the average grain size after holding at 950 °C increases slightly. Almost no recrystallization is observed after the first-pass deformation at 750 °C, and the small grains observed in Figure 7c,d are all the SRX grains that formed during the holding stage. The LAGBs content increases as the first-pass deformation temperature increases. These different microstructures change the recrystallization behavior during subsequent deformation.

### 3.4. Microstructural Characteristics after Second-Pass Compression (Stage-D2)

Figure 8 shows the microstructures at the beginning of the secondary deformation (before peak strain). The growth of the  $\beta$  grains is very rapid during hot working, and the grains grow to large sizes at the beginning of the deformation. In the sample first compressed at 700 °C and then second-pass deformed at 950 °C, CDRX is the main restoration mechanism in the early stage of deformation (square area in Figure 8a). This phenomenon has also been observed in 304 austenitic stainless steel [19] when the initial grain size decreased from 35  $\mu\text{m}$  to 8  $\mu\text{m}$ . Since CDRX requires less energy than DDRX, it occurs sooner. A small amount of DDRX occurs at grain boundaries (shown in the circled area). The occurrence of these two kinds of recrystallization significantly increases the LAGB fraction compared with the previous stage.

As for the samples subjected to first-pass compression at other temperatures, CDRX in the matrix almost disappears and a small amount of DDRX appears at the grain boundaries (circled in Figure 8d). The  $\beta$  grain morphology does not change much after deformation. Meanwhile, the LAGB content is significantly reduced compared with the previous stage. Generally speaking, the LAGB content should increase upon increasing the strain, and a slight increase in the LAGB content should be observed after the early deformation stage. This is because some of the residual LAGBs are preferentially transformed into HAGBs during the early stage of second-pass deformation.

The grain morphology and KAM maps after the second-pass deformation are shown in Figure 9. The morphology and grain size of the  $\beta$  matrix change significantly after deformation. Perpendicular to the direction of compression,  $\beta$  grains are elongated and grain boundaries are serrated. Discontinuous dynamic recrystallized grains are observed at the junctions of grain boundaries, and they form by bulging out from grain boundaries as non-deformed new grains, as circled in Figure 9. The recrystallized grain size is independent of the grain size before deformation [31]. After first-pass compression at a lower temperature, the volume fraction of the recrystallized grains is higher due to the grain refinement during the  $\beta$  holding stage. As a high-energy region, grain boundaries promote recrystallization nucleation and fine grains have more grain boundaries than coarse grains [20].

In the sample that was first compressed at 700 °C and then secondarily deformed at 950 °C (Figure 9a), dislocations preferentially accumulate at grain boundaries during second-pass deformation, and grain growth occurs simultaneously. Then, the LAGBs formed by dislocations entanglement stay in their original locations, which leads to LAGBs becoming uniformly distributed within the matrix. The KAM map shows the uniform dislocation density distribution. In the samples first compressed at 750–850 °C then secondarily deformed at 950 °C (Figure 9b–d), the density of the dislocations decreases and is non-uniformly distributed.

Meanwhile, many substructures form in  $\beta$  grains after the second compression. LAGBs are mainly concentrated at locations with a high dislocation density, such as  $\beta$  grain boundaries. During the early stage of second deformation, partial deformation energy is consumed, and the number of LAGBs generated by the remaining deformation energy decreases; therefore, after second-pass deformation, the number of LAGBs increases but the LAGB content decreases obviously with the increase in the first deformation temperature. CDRX requires less energy than DDRX, and it is mainly observed in fine grains; thus, the LAGB fraction of the samples subjected to first-pass compression at 700 °C is the highest, and the LAGB content decreases upon increasing the first-pass compression temperature.

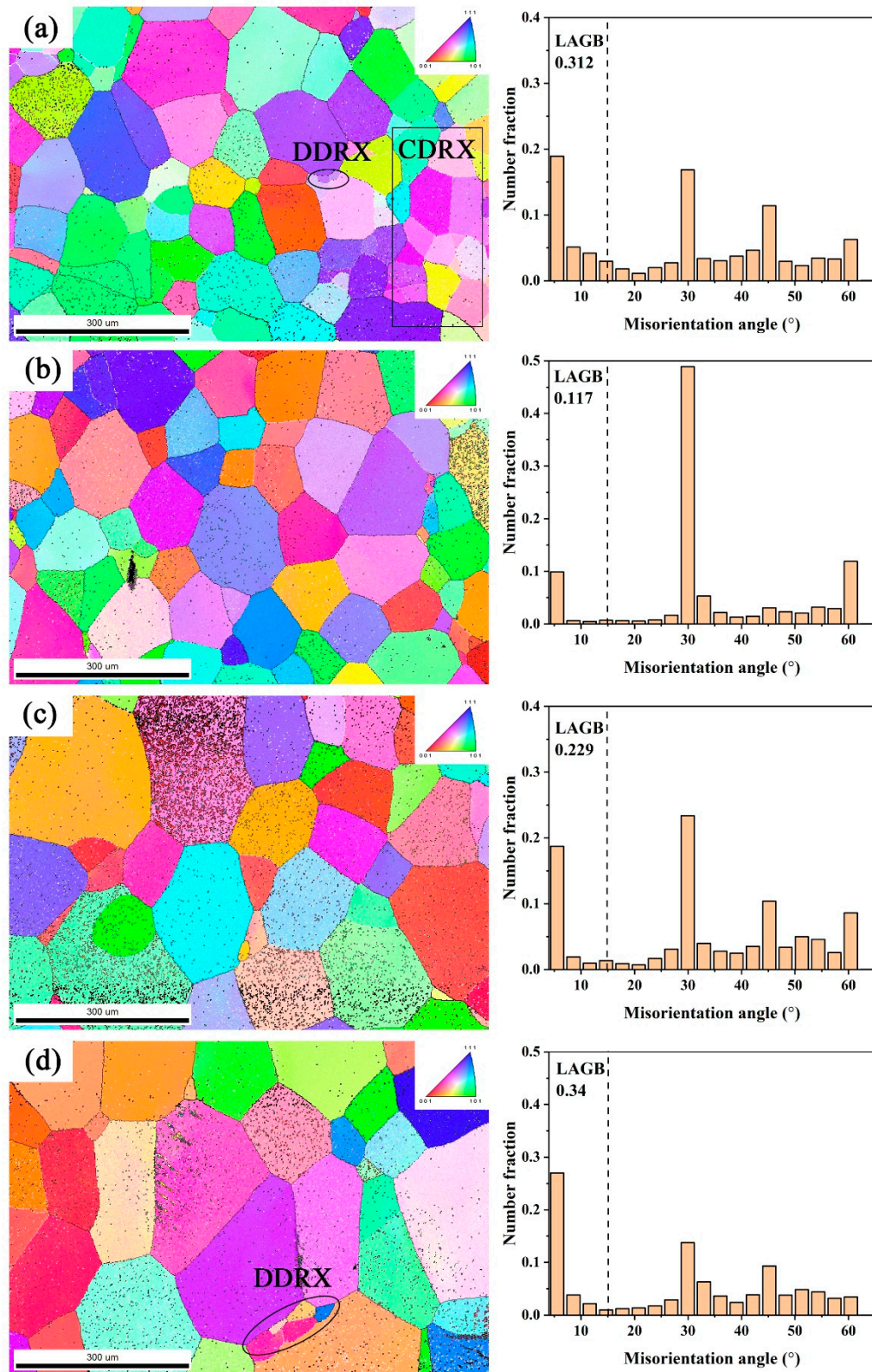


**Figure 8.** EBSD figures of samples after secondary-pass compression at 950 °C with 0.02 strain with the first-pass deformation temperature of (a) 700 °C, (b) 750 °C, (c) 800 °C, (d) 850 °C.

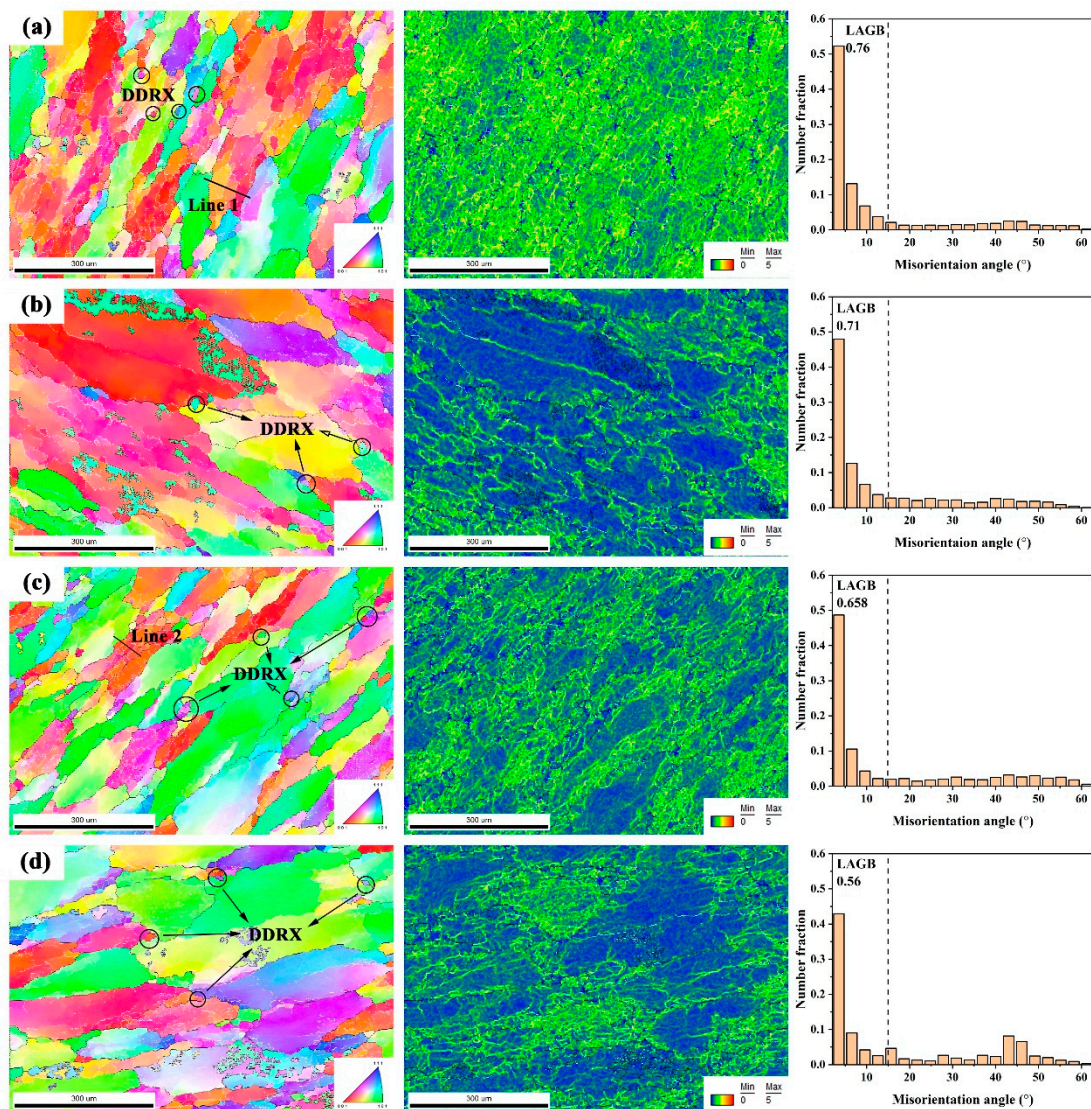


**Figure 9.** EBSD and KAM figures of samples after second compression at 950 °C with 0.56 strain and a first-pass deformation temperature of (a) 700 °C, (b) 750 °C, (c) 800 °C, (d) 850 °C.

There are two deformation modes of CDRX in the  $\beta$  region after deformation (line 1 and line 2 in Figure 9a,c). The first is the formation of new subgrains that are relatively uniformly distributed in the matrix. HAGBs formed after recrystallization cannot form in the case of insufficient strain, which leads to the formation of substructures and a higher dislocation density in the matrix [33]. Continuous dynamic recrystallization has no obvious nucleation and growth process but is accomplished by the continuous rotation of sub-crystals at grain boundaries [34]. This is shown in Figure 9 L1, and the orientation change is shown in Figure 10. According to the grain orientation difference, this region is divided into five parts. The point-to-point misorientation from region B to region D is a low angle of  $<15^\circ$ . Since the dislocation density is homogeneously distributed within the grains, subgrains are formed in the original grain at the same time and have similar sizes and similar misorientations. This leads to only a small change in the point-to-original misorientation between regions B, C, and D. These subgrains are mainly distributed parallel to the compression axis.

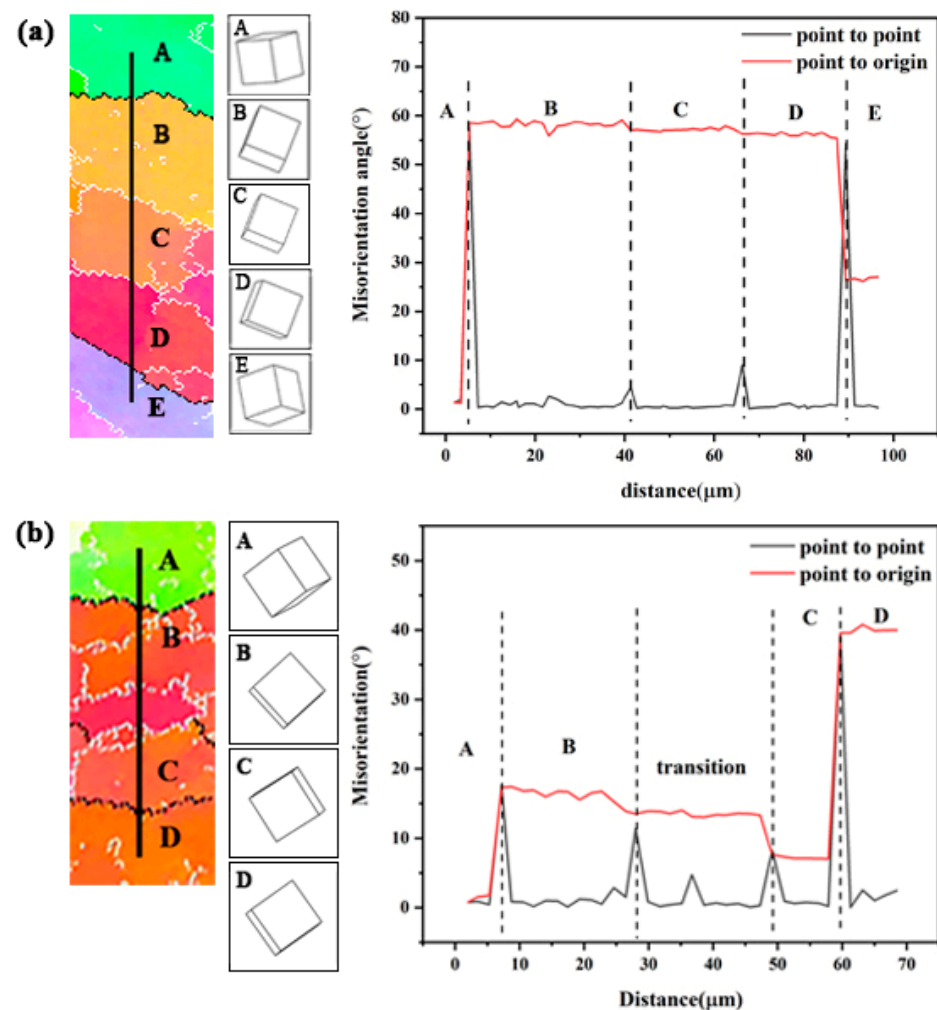


**Figure 10.** Orientation change along (a) line 1 and (b) line 2.

The second deformation mode is the continuous transformation from LAGBs to HAGBs, which occurs non-uniformly in the material. After deforming at 950 °C with 0.56 strain, some grain boundaries are observed in the matrix. These grain boundaries that are perpendicular to the deformation direction divide the original grains into several substructures to form grain-scale deformation bands [15,35]. These characteristics are markedly different from those of the substructures formed in the first mode. Point-to-original misorientation decreases in a gradient, and there is an obvious transformation region between regions B and C, in which misorientations undergo an obvious change. The EBSD figures in L2 indicate that this is a continuous process, and the boundaries between the transformation regions B and C are composed of alternating LAGBs and HAGBs. Non-uniform dislocation in the sample is an important reason for the formation of deformation bands, which are more easily observed in the coarse initial grains. Since deformation bands are mainly distributed at grain boundaries with severe deformation, more substructures are formed by this mode than the first mode.

#### 4. Conclusions

In this study, the deformation behavior and microstructure of Ti-55511 alloy during two-pass thermal compression were investigated. The conclusions can be summarized as follows:

- (1) The peak stress during first-pass deformation decreases upon increasing the deformation temperature. The peak stress during second-pass deformation increases upon increasing the first-pass deformation temperature.
- (2) During first-pass compression, the dominant restoration mechanisms are DRX and DRV at 700 °C with lamellar  $\alpha$  phase in the matrix. At higher deformation temperatures, lamellar  $\alpha$  phase disappears and deformation is dominated by the recovery mechanism. Meanwhile, the level of recovery decreases at higher deformation temperatures.
- (3) During the holding stage at 950 °C for 3 min, the average  $\beta$  grain size decreases upon decreasing the first-pass deformation temperature. When the first-pass deformation temperature is 700 °C, the dislocation density decreases due to recrystallization, the grain growth rate becomes slower, and the grain refinement is obvious.
- (4) Two restoration mechanisms co-exist during second-pass deformation: CDRX and DDRX. At the beginning of the deformation, residual LAGBs formed during first-pass deformation preferentially transform to HAGBs. Then, CDRX is observed in initial fine grains but it is not observed in the initial coarse grains. Meanwhile, a small amount of DDRX is observed at grain boundaries.
- (5) The CDRX behavior during second-pass deformation is affected by the grain size. The formation of substructures is related to the grain size before deformation. The substructures in the initial fine grains form at the same time and have the same misorientation angle as the original grains. The substructures in the initial coarse grains are formed by deformation bands and gradually transform from a non-uniform deformation region. The misorientation angle displays a gradient to the original grains, which is closely related to the dislocation density distribution.

**Author Contributions:** Data curation, H.W. and J.G.; Writing—original draft preparation, H.W.; Writing—review and editing, H.W. and X.Z.; Supervision, K.Z.; Project Administration, K.Z. and C.C.; Funding Acquisition, X.Z. and K.Z. All authors have read and agreed to the published version of the manuscript.

**Funding:** The authors are grateful to thanks to funding support from the National Natural Science Foundation of China (No. 51871242), the National Key R&D Program of China (2018YFB0704100) and Scientific and Technological Innovation Projects of Hunan Province, China (No. 2017GK2292).

**Data Availability Statement:** All the raw data supporting the conclusion of this paper were provided by the authors.

**Acknowledgments:** The authors would like to acknowledge financial support from the National Natural Science Foundation of China (No. 51871242); Scientific and Technological Innovation Projects of Hunan Province, China (No. 2017GK2292); and the National Key R&D Program of China (2018YFB0704100). Besides this, the authors would like to thank Jinyang Ge for assistance with the experiments.

**Conflicts of Interest:** The authors declare that they have no known competing financial interests or personal relationships that could have appeared to influence the work reported in this paper.

## References

1. Li, C.; Zhang, X.Y.; Zhou, K.C.; Peng, C.Q. Relationship between lamellar  $\alpha$  evolution and flow behavior during isothermal deformation of Ti-5Al-5Mo-5V-1Cr-1Fe near  $\beta$  titanium alloy. *Mater. Sci. Eng. A* **2012**, *558*, 668–674. [[CrossRef](#)]
2. Tsybanev, G.V.; Ageev, M.A.; Titarenko, R.V. Analysis of the specific features of the elements of landing gears of aircrafts aimed at the evaluation of the load-bearing capacity of the structure. *Strength Mater.* **2008**, *40*, 458–462. [[CrossRef](#)]
3. Banerjee, D.; Williams, J.C. Perspectives on titanium science and technology. *Acta Mater.* **2013**, *61*, 844–879. [[CrossRef](#)]
4. Zhou, W.; Ge, P.; Zhao, Y.; Wu, H.; Li, Q.; Chen, J. Response of heat-treatment on A near- $\beta$  titanium alloy. *Xiyou Jinshu Cailiao Yu Gongcheng/Rare Met. Mater. Eng.* **2010**, *39*, 723–726.
5. Ravichandran, K.S. Fracture mode transitions during fatigue crack growth in Ti-6Al-4V alloy. *Scr. Metall. Mater.* **1990**, *24*, 1275–1280. [[CrossRef](#)]
6. Estrin, Y.; Vinogradov, A. Extreme grain refinement by severe plastic deformation: A wealth of challenging science. *Acta Mater.* **2013**, *61*, 782–817. [[CrossRef](#)]

7. Wang, B.; Wang, X.; Li, J. Formation and Microstructure of Ultrafine-Grained Titanium Processed by Multi-Directional Forging. *J. Mater. Eng. Perform.* **2016**, *25*, 2521–2527. [[CrossRef](#)]
8. Fan, X.G.; Zhang, Y.; Zheng, H.J.; Zhang, Z.Q.; Gao, P.F.; Zhan, M. Pre-processing related recrystallization behavior in  $\beta$  annealing of a near- $\beta$  Ti-5Al-5Mo-5V-3Cr-1Zr titanium alloy. *Mater. Charact.* **2018**, *137*, 151–161. [[CrossRef](#)]
9. Mironov, S.; Murzinova, M.; Zharebtsov, S.; Salishchev, G.A.; Semiatin, S.L. Microstructure evolution during warm working of Ti-6Al-4V with a colony- $\alpha$  microstructure. *Acta Mater.* **2009**, *57*, 2470–2481. [[CrossRef](#)]
10. Zharebtsov, S.; Kudryavtsev, E.; Kostjuchenko, S.; Malysheva, S.; Salishchev, G. Strength and ductility-related properties of ultrafine grained two-phase titanium alloy produced by warm multiaxial forging. *Mater. Sci. Eng. A* **2012**, *536*, 190–196. [[CrossRef](#)]
11. Bézi, Z.; Krállics, G.; El-Tahawy, M.; Pekker, P.; Gubicza, J. Processing of ultrafine-grained titanium with high strength and good ductility by a combination of multiple forging and rolling. *Mater. Sci. Eng. A* **2017**, *688*, 210–217. [[CrossRef](#)]
12. Jia, J.; Zhang, K.; Lu, Z. Dynamic recrystallization kinetics of a powder metallurgy Ti-22Al-25Nb alloy during hot compression. *Mater. Sci. Eng. A* **2014**, *607*, 630–639. [[CrossRef](#)]
13. Warchomicka, F.; Poletti, C.; Stockinger, M. Study of the hot deformation behavior in Ti-5Al-5Mo-5V-3Cr-1Zr. *Mater. Sci. Eng. A* **2011**, *528*, 8277–8285. [[CrossRef](#)]
14. Hu, Z.; Zhou, X.; Nie, X.A.; Zhao, S.; Liu, H.; Yi, D.; Zhang, X. Finer subgrain microstructure induced by multi-pass compression in  $\alpha+\beta$  phase region in a near- $\beta$  Ti-5Al-5Mo-5V-1Cr-1Fe alloy. *J. Alloys Compd.* **2019**, *788*, 136–147. [[CrossRef](#)]
15. Fan, X.G.; Zhang, Y.; Gao, P.F.; Lei, Z.N.; Zhan, M. Deformation behavior and microstructure evolution during hot working of a coarse-grained Ti-5Al-5Mo-5V-3Cr-1Zr titanium alloy in beta phase field. *Mater. Sci. Eng. A* **2017**, *694*, 24–32. [[CrossRef](#)]
16. Wang, K.; Li, M.Q. Flow behavior and deformation mechanism in the isothermal compression of the TC8 titanium alloy. *Mater. Sci. Eng. A* **2014**, *600*, 122–128. [[CrossRef](#)]
17. Ning, Y.Q.; Luo, X.; Liang, H.Q.; Guo, H.Z.; Zhang, J.L.; Tan, K. Competition between dynamic recovery and recrystallization during hot deformation for TC18 titanium alloy. *Mater. Sci. Eng. A* **2015**, *635*, 77–85. [[CrossRef](#)]
18. Wu, W.X.; Jin, L.; Dong, J.; Zhang, Z.Y.; Ding, W.J. Effect of initial microstructure on the dynamic recrystallization behavior of Mg-Gd-Y-Zr alloy. *Mater. Sci. Eng. A* **2012**, *556*, 519–525. [[CrossRef](#)]
19. Dehghan-Manshadi, A.; Hodgson, P.D. Dependency of recrystallization mechanism to the initial grain size. *Metall. Mater. Trans. A Phys. Metall. Mater. Sci.* **2008**, *39*, 2830–2840. [[CrossRef](#)]
20. Lütjering, G.; Williams, J.C. *Titanium*, 2nd ed.; Springer: Berlin, Germany, 2007; pp. 72–79.
21. Dikovits, M.; Poletti, C.; Warchomicka, F. Deformation mechanisms in the near- $\beta$  titanium alloy Ti-55531. *Metall. Mater. Trans. A Phys. Metall. Mater. Sci.* **2014**, *45*. [[CrossRef](#)]
22. Balachandran, S.; Kumar, S.; Banerjee, D. On recrystallization of the  $\alpha$  and  $\beta$  phases in titanium alloys. *Acta Mater.* **2017**, *131*, 423–434. [[CrossRef](#)]
23. Wagner, F.; Bozzolo, N.; Van Landuyt, O.; Grosdidier, T. Evolution of recrystallisation texture and microstructure in low alloyed titanium sheets. *Acta Mater.* **2002**, *50*, 1245–1259. [[CrossRef](#)]
24. Chen, W.; Lv, Y.; Zhang, X.; Chen, C.; Lin, Y.C.; Zhou, K. Comparing the evolution and deformation mechanisms of lamellar and equiaxed microstructures in near  $\beta$ -Ti alloys during hot deformation. *Mater. Sci. Eng. A* **2019**, *758*, 71–78. [[CrossRef](#)]
25. Tang, B.; Xiang, L.; Yan, Z.; Kou, H.; Li, J. Effect of strain distribution on the evolution of  $\alpha$  phase and texture for dual-phase titanium alloy during multi-pass forging process. *Mater. Chem. Phys.* **2019**, *228*, 318–324. [[CrossRef](#)]
26. Li, L.; Luo, J.; Yan, J.J.; Li, M.Q. Dynamic globalization and restoration mechanism of Ti-5Al-2Sn-2Zr-4Mo-4Cr alloy during isothermal compression. *J. Alloys Compd.* **2015**, *622*, 174–183. [[CrossRef](#)]
27. Li, L.X.; Lou, Y.; Yang, L.B.; Peng, D.S.; Rao, K.P. Flow stress behavior and deformation characteristics of Ti-3Al-5V-5Mo compressed at elevated temperatures. *Mater. Des.* **2002**, *23*, 451–457. [[CrossRef](#)]
28. Jia, W.; Zeng, W.; Zhou, Y.; Liu, J.; Wang, Q. High-temperature deformation behavior of Ti60 titanium alloy. *Mater. Sci. Eng. A* **2011**, *528*, 4068–4074. [[CrossRef](#)]
29. Huang, Y.; Humphreys, F.J. Transient dynamic recrystallization in an aluminum alloy subjected to large reductions in strain rate. *Acta Mater.* **1997**, *45*, 4491–4503. [[CrossRef](#)]
30. Cram, D.G.; Zurob, H.S.; Brechet, Y.J.M.; Hutchinson, C.R. Modelling discontinuous dynamic recrystallization using a physically based model for nucleation. *Mater. Sci. Forum* **2012**, *715–716*, 492–497. [[CrossRef](#)]
31. Huang, K.; Logé, R.E. A review of dynamic recrystallization phenomena in metallic materials. *Mater. Des.* **2016**, *111*, 548–574. [[CrossRef](#)]
32. Vandermeer, R.A.; Jensen, D.J.; Woldt, E. Grain boundary mobility during recrystallization of copper. *Metall. Mater. Trans. A Phys. Metall. Mater. Sci.* **1997**, *28*, 749–754. [[CrossRef](#)]
33. Xiang, L.; Tang, B.; Xue, X.; Kou, H.; Li, J. Characteristics of the dynamic recrystallization behavior of Ti-45Al-8.5Nb-0.2W-0.2B-0.3Y alloy during high temperature deformation. *Metals* **2017**, *7*, 261. [[CrossRef](#)]
34. Tikhonova, M.; Kaibyshev, R.; Fang, X.; Wang, W.; Belyakov, A. Grain boundary assembles developed in an austenitic stainless steel during large strain warm working. *Mater. Charact.* **2012**, *70*, 14–20. [[CrossRef](#)]
35. Kuhlmann-Wilsdorf, D. Overview No. 131: “regular” deformation bands (DBs) and the leds hypothesis. *Acta Mater.* **1999**, *47*. [[CrossRef](#)]